*Keynote Speech*

# Nanomaterials as a green multifunctional material for water purification and energy applications

## Prof. Ruey-an Doong

*Institute of Analytical and Environmental Sciences, National Tsing Hua University, Taiwan*

## Introduction

Nanomaterials are novel materials which can not only serve as a photoelectrochhemical catalyst but also as an electrode material because of their suitable band gap, high surface area. Two-dimensional (2D) materials such as graphene family and mesoporous carbon nitride ($C_3N_4$) have recently attracted considerable interest because of high surface area, appropriate chemical anchoring sites, large pore size/volume, good electrical conductivity, and thermal stability [1-4]. Among these materials, graphitic carbon nitride (g-$C_3N_4$), an organic polymeric semiconductor mainly consisting of carbon and nitrogen with a band gap of 2.7 eV, exhibits high thermal and chemical stability, excellent electron transfer ability, and easy recycling, and has been commonly used as a photocatalyst for the effective decomposition of various hazardous chemicals. Furthermore, g-$C_3N_4$ has been successfully utilized as a support to disperse and stabilize metal nanoparticles such as Pd, Pt, Cu, and Co. Basically, g-$C_3N_4$ is formed by the linkage of N bridged tri-s-triazine repeating unit, which is generated by two-dimensional conjugated planes packed together via van der Waals interactions. In view of its unique structure and preponderance, g-$C_3N_4$ has been widely employed in a wide variety of fields such as oxygen reduction reaction, photocatalysis, photoelectrochemical reaction, and sensor.

For heterogeneous (photo) catalytic processes, organic compounds and metal derivatives could bind or intercalate into the matrix of g-$C_3N_4$ through the surface anchoring sites to improve the (photo) catalytic reaction rate, and thus broaden the (photoelectro) catalytic application of g-$C_3N_4$ toward organic decomposition. The unique architecture of g-$C_3N_4$ and the outstanding (photo) catalytic performance of metal and metal oxide nanoparticles such as Au, $CeO_2$, and graphene quantum dots (GQDs) provide a great impetus to use g-$C_3N_4$ as a promising support to judiciously decorate metal/metal oxide for the formation of highly active and green heterogeneous (photo) catalyst. Herein, we report the facile synthesis of mesoporous carbon nitride with ordered, uniform channel morphology and their use as a photocatalyst to decompose pharmaceuticals as well as a support for metal/metal oxide nanoparticles to catalytically reduce nitroarenes as well as for energy storage.
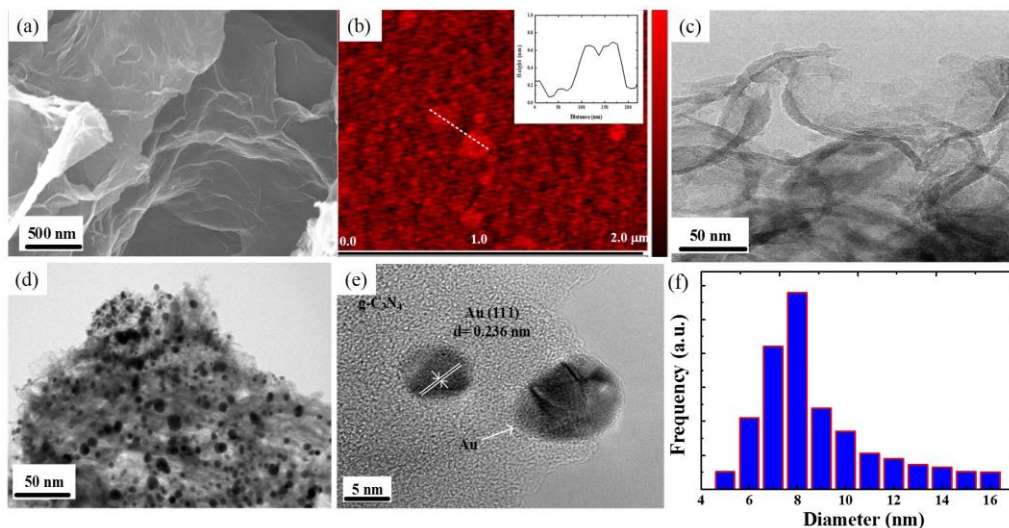
**Fig. 1.** (a)SEM, (b) AFM, and (c) TEM images of as-prepared g-$C_3N_4$ nanosheets; (d) TEM and (e) HRTEM images of Au@g-$C_3N_4$ nanocomposites, and (f) histogram of Au particle size distribution in Au@g-$C_3N_4$ nanocomposites.

## Reduction of nitroarene over Au/g-$C_3N_4$

The morphology as well as the particle size distribution of as-prepared g-$C_3N_4$ nanosheets and Au@g-$C_3N_4$ nanocomposites are examined. **Fig. 1a** shows the SEM image of the exfoliated g-$C_3N_4$. The typical 2-D structure interconnected with wrinkled g-$C_3N_4$ nanosheets is observed vividly, indicating the successful split of bulk $C_3N_4$ layers into small and thin nanosheets via thermal exfoliation. The AFM image displays that the g-$C_3N_4$ nanosheets are well separated (**Fig. 1b**) with a thickness of *ca*. 0.7 nm (Inset of **Fig. 1b**), indicating the successful exfoliation of bulk g-$C_3N_4$ into 3–6 layers of $C_3N_4$ nanosheets. The TEM image (**Fig. 1c**) shows the lamellar structure of g-$C_3N_4$, which is formed by the linkage of graphitic-like planes. After loading 2 wt% of Au NPs, a homogeneous distribution of Au NPs on the g-$C_3N_4$ nanosheets is clearly observed in the TEM image (**Fig. 1d**), depicting the successful formation of Au@g-$C_3N_4$ nanocomposites. The HRTEM image clearly shows the characteristic lattice fringe with crystal plane distance of 0.236 nm (**Fig. 1e**), which corresponds to the (111) plane of face centered cubic (fcc) Au NPs. The strong interfacial interaction between Au NP and g-$C_3N_4$ layer is also observed in the HRTEM image, and is conducive to the electron transfer processes. Furthermore, the particle size distribution of Au NPs on g-$C_3N_4$ can be calculated from the histogram analysis, and the Au NPs on the g-$C_3N_4$ nanosheets are in the range of 5−15 nm with a mean diameter of 8 nm (**Fig. 1f**). The particle size of Au NPs on

Faculty of Science
University of Ruhuna

RISTCON
2020

g-$C_3N_4$ is smaller than that of Au NPs alone (18 nm), indicating that the g-$C_3N_4$ nanosheet is an excellent support to homogeneously disperse Au NPs that constrains the growth of Au NPs.

**Fig. 2** shows the mass loading effect of Au NPs in Au@g-$C_3N_4$ on the catalytic reduction efficiency of 4-NP in the presence of 7 mM $NaBH_4$. It is clear that g-$C_3N_4$ is catalytically inactive on the reduction of 4-NP. Although the reaction of 4-NP ($E^0$ ($_{4-NP/4-AP}$) = −0.76 V) with $NaBH_4$ (= −1.33 V) is thermodynamically favorable, the reduction of 4-NP by $NaBH_4$ is kinetically slow. Addition of Au NPs significantly enhances the reduction efficiency and rate of 4-NP over Au@g-$C_3N_4$ in the presence of $NaBH_4$. The reduction of 4-NP to 4-amnophenol increases from 66 to > 99% when the Au loading increases from 0.5 to 2 wt%, and then slightly decreases to 96% at 3 wt% after 10 min of reaction. The pseudo-first-order rate constant ($k_{obs}$) for 4-nitrophenol reduction is $1.83 \times 10^{-3}$ ($r^2 = 0.998$), $3.07 \times 10^{-3}$ ($r^2 = 0.995$), $1.50 \times 10^{-2}$ ($r^2 = 0.983$), and $5.33 \times 10^{-3}$ sec$^{-1}$ ($r^2 = 0.997$), respectively, over the 0.5-, 1-, 2- and 3-wt% Au@g-$C_3N_4$. When normalized to the specific surface area of Au@g-$C_3N_4$, the normalized surface rate constant ($k_m$) for 4-NP reduction increases from 3.24 to 20.25 min$^{-1}$ m$^{-2}$ at 0.5 – 2-wt% Au@g-$C_3N_4$ and then decreases to 6.78 min$^1$ m$^{-2}$ at 3-wt% Au@g-$C_3N_4$, indicating that 2-wt% Au@g-$C_3N_4$ provides optimal active sites for both $NaBH_4$ and 4-NP to exhibit the best catalytic activity in comparison with other Au loadings of Au@g-$C_3N_4$.
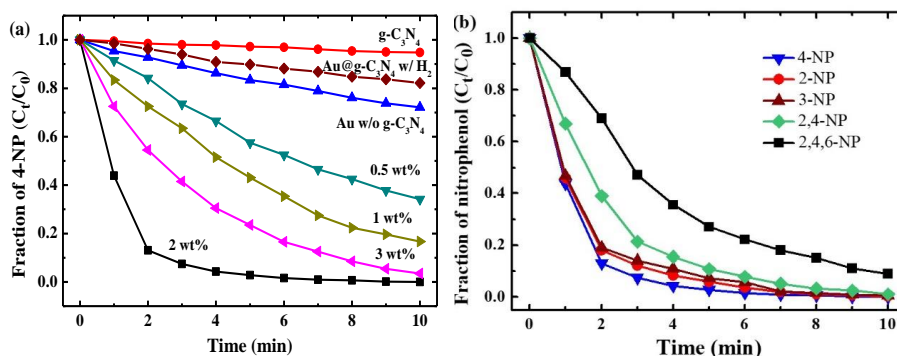


**Fig. 2.** (a) Effect of Au content on the reduction of 4-NP and (b) catalytic reduction of various nitrophenol compounds by Au@g-$C_3N_4$ nanocatalyst in the presence of $NaBH_4$.

To further understand the applicability of Au@g-$C_3N_4$ nanocomposite to catalyze the reduction of nitrophenol, several nitroaromatics including 2-NP, 3-NP, 4-NP, 2,4-DNP and 2,4,6-TNP are selected as the target compounds. As shown in **Fig. 2b**, the Au@g-$C_3N_4$ nanocomposite exhibits remarkable catalytic activity toward nitrophenol reduction by $NaBH_4$. Both the $k_{obs}$ and normalized

surface rate constants of nitrophenol reduction follow the order: 4-NP > 2-NP > 3-NP > 2,4-DNP > 2,4,6-TNP, indicating 4-NP reduction the most favorable over Au@g-C$_3$N$_4$ nanocatalyst. The rate constant of nitrophenol reduction decreases with the increase in number of nitro-substituent, which is mainly attributed to the molecular hindrance and steric effect of nitroaromatics to penetrate into the catalyst network.

## Photodegradation of pharmaceuticals over I, K-codopedd g-C$_3$N$_4$

Not just only shows the superior catalytic capability toward nitroarenes reduction, g-C3N4 also exhibit the excellent photocatalytic activity toward pharmaceuticals degradation. We have proposed a simple method to fabricate visible-light responsive iodine- and potassium-codoped for sulfamethoxazole (SMX) photodegradation. As shown in **Fig. 3a**. The)for SMX photodegradation were computed at 0.027, 0.035 and 0.106 min$^{-1}$ at doping temperature of 450, 500 and 530 °C, respectively. The k$_{obs}$ for SMX photodegradation by IK-C$_3$N$_4$ at 530 °C was 4 times higher than that at 450 °C. The increased reaction rate at high doping temperature is mainly attributed to the enhanced exfoliation and doping efficiency, resulting in the acceleration of photocatalytic performance towards SMX removal.
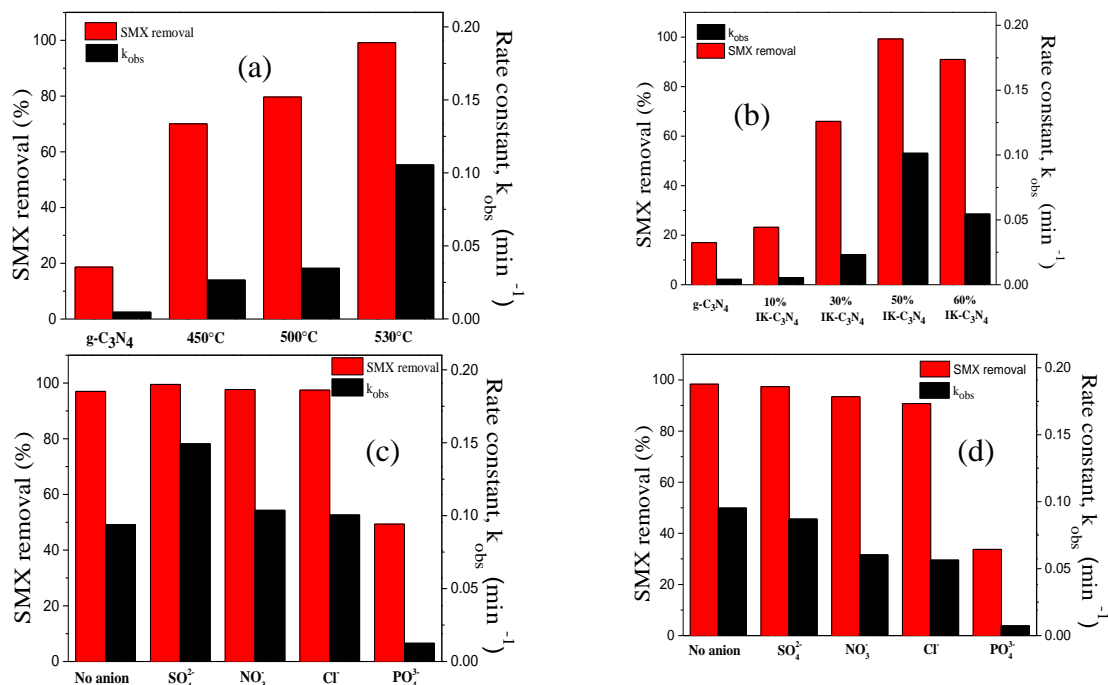
**Fig. 3** Pseudo-first order kinetic rate constants and SMX degradation rate by as-synthesized photocatalysts under visible light irradiation at varying (a) calcination temperature, (b) dopant amount (c) 0.01 M anion, and (d) 0.05 M anions.

**Fig. 3b** shows that g-$C_3N_4$ has a slight photocatalytic activity toward SMX degradation and only 17.0% of SMX is photodegraded after 45 min of irradiation. In the absence of any photocatalyst, less than 2% of SMX is photodegraded under the visible light irradiation, indicating that the direct photolysis of SMX can be neglected. Nevertheless, all doped IK-$C_3N_4$ photocatalysts had better photocatalytic performance compared to pure g-$C_3N_4$ and the varying dopant amounts of IK-$C_3N_4$ composites exhibited different SMX photodegradation efficiencies. The degradation efficiency of SMX by IK-$C_3N_4$ follows the order: 50 wt% > 60 wt% > 30 wt% > 10 wt% **>** as-prepared g-$C_3N_4$ and increases from 23.2 % at 10 wt% to > 99% at 50 wt%. The superior photocatalytic performance of 50 wt% IK-$C_3N_4$ is mainly attributed to the homogenous dispersion and lattice defects caused by the co-doping of I and K into the g-$C_3N_4$ nanosheet that promotes good charge transfer and separation of $e^-/h^+$ pairs, which have been shown in PL spectra. In addition, the high specific surface area and pore volume provide more reactive sites for 50 wt% IK-$C_3N_4$ for the enhanced photocatalytic degradation efficiency. Also shown in **Fig. 3b**, the $k_{obs}$ for SMX photodegradation value increases from 0.0055 $min^{-1}$ for 10 wt% IK-$C_3N_4$ to 0.1014 $min^{-1}$ for 50 wt% IK-$C_3N_4$ and then decreases to 0.0545 $min^{-1}$ for 60 wt% IK-$C_3N_4$. The decline in photocatalytic activity is attributed to the shielding effect caused by extra defects at high dopant concentrations. The $k_{obs}$ value of 50 wt% IK-$C_3N_4$ is 24.1 times higher than that of g-$C_3N_4$ (0.0042 $min^{-1}$), showing that the former is a superior visible-light-responsive photocatalyst for SMX photodegradation.

Inorganic salts are commonly found in actual water and wastewater samples. Therefore, the impact of anionic species on the photodegradation of SMX by 50 wt% IK-$C_3N_4$ was also examined in this study. The addition of 0.01 M anion (phosphate, sulfate, nitrate and chloride) to the water matrix enhanced SMX photodegradation efficiency for each of the anions except for $PO_4^{3-}$ (**Fig. 3c**). The enhancement in SMX photodegradation efficiency follows the order: $SO_4^{2-}$ > $NO_3^-$ > $Cl^-$. Sulfate anions promote photodegradation since it is known to react with photogenerated holes generating other oxidizing radical and instigate the formation of ·OH radicals after reacting with $H_2O$ molecules. The $k_{obs}$ for SMX photodegradation was found at 0.1493, 0.1037 and 0.1005 $min^{-1}$ in the presence of 0.01 M $SO_4^{2-}$, $NO_3^-$ and $Cl^-$, respectively which is 1.07 – 1.59 times higher than the control run (without anion). The observed increase in the reaction rate is ascribed to the transformation of the anions into radical species

that promoted the separation of the electron and hole pairs in an electrostatic field created on the surface of the photocatalyst. At higher anion concentration of 0.05 M, however, detrimental results were obtained for all anions. In **Fig. 3d,** the photodegradation efficiencies of SMX were 34, 91 and 93% and $k_{obs}$ values of 0.0073, 0.0564 and 0.0604 $min^{-1}$ for $PO_4^{3-}$, $Cl^-$ and $NO_3^-$, respectively, after 45 min of irradiation. Although a nearly complete SMX photodegradation was found in the presence of 0.05 M $SO_4^{2-}$, the $k_{obs}$ for SMX photodegradation was at 0.0871 $min^{-1}$, which is 1.09 times lower than that in the absence of anions. The difference in anion concentration affects SMX photodegradation due to the fact that at high concentration, they serve as OH radical scavengers consequently terminating radical formation [50] Thus, competition between SMX and anions for photogenerated holes and electrons resulted in the decrease in SMX photodegradation rate and efficiency. Moreover, phosphate anions are unique by consistently giving unfavorable effect during SMX photodegradation regardless of the anion concentration. This is mainly due to the decrease in adsorption of SMX onto the $IK-C_3N_4$ surface whenever there is sodium phosphate.
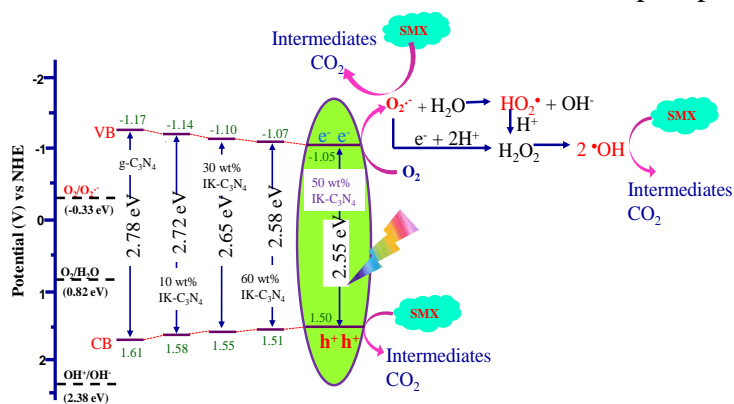


**Fig. 4** The relationship of CB and VB position of various loading amounts of $IK-C_3N_4$ and the possible reaction mechanism for SMX photodegradation by $IK-C_3N_4$ under visible light irradiation.

The reaction mechanisms for SMX photodegradation by visible-light-responsive $IK-C_3N_4$ is also proposed. As shown in **Fig. 4**, the irradiation of $IK-C_3N_4$ with visible light would excite the electron from VB to CB and produce $e^-$-$h^+$ pairs. The electron in CB would react with oxygen ($O_2$) in aqueous solution to produce superoxide anion radicals ($O_2^{•-}$) [2]. The superoxide anion radicals will undergo the chain reaction to generate hydrogen peroxyl radicals ($HO_2^•$), hydrogen peroxide ($H_2O_2$) and hydroxyl radicals ($^•OH$). Those photogenerated radicals and hole ($h^+$) can serve as the oxidizing agents to decompose pollutants, results in the acceleration of photocatalytic degradation efficiency and rate of SMX. It

is noteworthy that the standard reduction potential of $^\bullet OH^+/^\bullet OH^-$ is at 2.38 eV vs. NHE, while the VB position of IK-C$_3$N$_4$ only locates 1.50 – 1.61 eV. This means that the hole generated from the visible light irradiation cannot trigger the generation of $^\bullet OH$ from the reduction reaction of O$_2$. Therefore, the hydroxyl radicals in the solution can only be obtained from the chain reactions of superoxide anion radicals. This result is in good agreement with the result of the scavenger experiment on which the reactive species that dominate the reaction is arranged in this manner O$_2^{\bullet -}$ > h$^+$ > $^\bullet$OH.

**Photodegradation of pharmaceuticals over CeO$_2$/IK-C3N4.**

Cerium oxide (CeO$_2$), an abundant rare-earth oxide, is a n-type photocatalyst with band gap of around 2.8 - 2.92 eV, which makes it highly capable of absorbing light in the visible spectrum. The combination of CeO$_2$ and IK-C$_3$N$_4$ can form direct Z-scheme n-n heterjunction for enhanced photodegradation. **Fig. 5a** shows the adsorption and photodegradation of acetaminophen (ACT) over various amount of CeO$_2$/IK-C$_3$N$_4$. Only 12% and 15% ACT removal by pure g-C$_3$N$_4$ and 15% CeO$_2$/ IK-C$_3$N$_4$ nanocomposite in 90 min of continuous mixing. Moreover, the enhanced ACT removal was observed immediately after visible light irradiation, which confirms that the ACT elimination is mainly due to the photocatalysis. Different CeO$_2$ loading over g-C$_3$N$_4$ were optimized for enhanced photocatalytic degradation of ACT (**Fig. 5b**). The 10% weight of CeO$_2$ was recorded with only 60% ACT degradation, 1.56 times higher than that of g-C$_3$N$_4$. The 15% CeO$_2$/ IK-C$_3$N$_4$ nanocomposite was found to be the optimal ratio wherein highest photocatalytic performance was observed. After 90 min of visible light irradiation, 98% of ACT was eliminated. This boost in performance is mainly caused by the balance of lattice defects introduced while suppresses the recombination of excitants from increased in area for surface charge. Meanwhile, further increase produces a surplus CeO$_2$ that competes for reactive sites, blocks $_{available}$ light energy and produces more defects that causes the decrease in performance. The 20% and 25% CeO$_2$ immobilization show only 91% and 94% removal efficiency, respectively in 90 min of reaction time. The ACT degradation rate is modelled by a pseudo-first-order reaction and the k$_{obs}$ values are 0.0101, 0.0386, 0.0312, 0.0266 and 0.0053 min$^{-1}$ for 10%, 15%, 20%, 25% CeO$_2$/IK-C$_3$N$_4$ and bare g-C$_3$N$_4$, respectively.
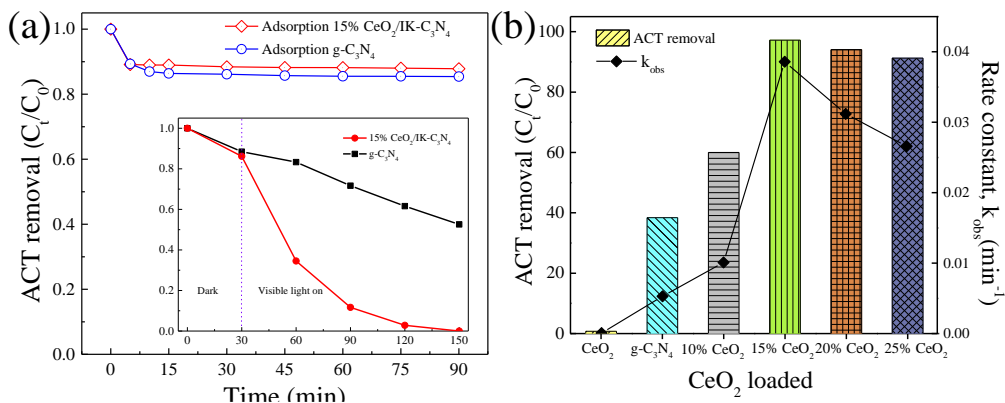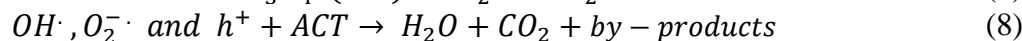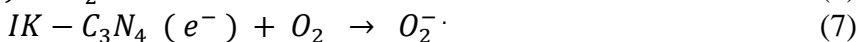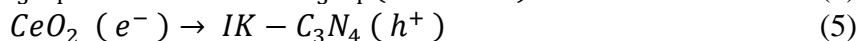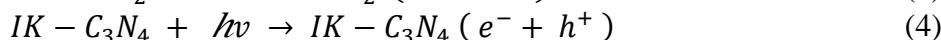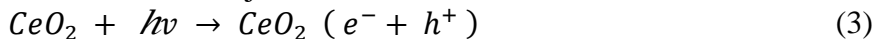
**Fig 4.** (a) Adsorption experiment, under visible light irradiation by 15% $CeO_2$/ IK-$C_3N_4$ nanocomposite and (b) corresponding first-order rate constant ($k_{obs}$) with different (b) $CeO_2$ loading on to the g-$C_3N_4$ catalysts.

In order to explain the degradation pathway performed by the photocatalytic system, the conduction band ($E_{CB}$) and valence band ($E_{VB}$) potentials of IK-$C_3N_4$ and $CeO_2$ was calculated by using the Mulliken electronegativity theory [2,3]:

$$E_{CB} = X - E_c + \frac{1}{2} E_g \qquad (1)$$

$$E_{VB} = E_{CB} - E_g \qquad (2)$$

where $X$ is the geometric mean of Mulliken electronegativity constituent atoms, $Ec$ is the hydrogen scale's energy of electrons (4.5 eV vs NHE) and $E_g$ is the band gap energy. The $X$ values are 4.72 eV for g-$C_3N_4$ and 5.56 eV for $CeO_2$. For IK-$C_3N_4$, the calculated $E_{CB}$ and $E_{VB}$ were -1.06 eV and 1.49 eV, respectively. The as-synthesized bare $CeO_2$ shows $E_{CB}$ and $E_{VB}$ equal to -0.43 eV and 2.55 eV. Based on the characterization, trapped radical species and calculated band structures, the probable charge carrier transfer path which helped to achieve the enhanced photodegradation by 15% $CeO_2$/ IK-$C_3N_4$ heterojunction (**Fig. 5**). The overlapping band energy levels of IK-$C_3N_4$ ($E_{CB} = -1.06, E_{VB} = 1.49$ ) and $CeO_2$ ( $E_{CB} = -0.43, E_{VB} = 2.55$ ), generated an effective structure for a heterojunction.

$$CeO_2 + h\nu \rightarrow CeO_2 \ (e^- + h^+) \qquad (3)$$

$$IK - C_3N_4 + h\nu \rightarrow IK - C_3N_4 \ (e^- + h^+) \qquad (4)$$

$$CeO_2 \ (e^-) \rightarrow IK - C_3N_4 \ (h^+) \qquad (5)$$

$$CeO_2 \ (h^+) + H_2O \rightarrow OH^\cdot \qquad (6)$$

$$IK - C_3N_4 \ (e^-) + O_2 \rightarrow O_2^- \cdot \qquad (7)$$

$$OH^\cdot, O_2^- \cdot \ and \ h^+ + ACT \rightarrow H_2O + CO_2 + by-products \qquad (8)$$

Under visible light irradiation, with enough photons to surpass the energy gap, both IK-$C_3N_4$ and $CeO_2$ produce photoexcited electron and hole pairs. Subsequently, the electrons are transported in the conduction band (CB) of $CeO_2$ to the valence band (VB) of IK-$C_3N_4$, Eq. (5) and holes left in VB of $CeO_2$ will produce •OH from $H_2O$, Eq. (6). The accumulated electrons that leaped to the CB will reduce the molecular oxygen to produce $O_2•^-$ immediately (Eq. (7)). Meanwhile, the holes left in the VB will interact with the organic molecules. Finally, the produced radical species of $O_2•^-$ and •OH will interact with the ACT molecules for degradation (Eq. (8)). On the basis of the scenarios mentioned, SEM/TEM topography image and XPS results, it is clearly that there is an interfacial interaction between the two semiconductors, and, thus, direct Z-scheme is achieved. The photogenerated e$^-$ with higher reduction potential are gathered on the CB of IK-$C_3N_4$ while the h$^+$ with higher oxidation potential remained on VB of $CeO_2$ which optimizes the redox potential of the heterojunction to intensify its degradation capabilities. Moreover, due to the transfer mechanism by Z-scheme, efficient transport of electrons from $CeO_2$ to g-$C_3N_4$ and suppress recombination of photo-generated pairs became achievable.
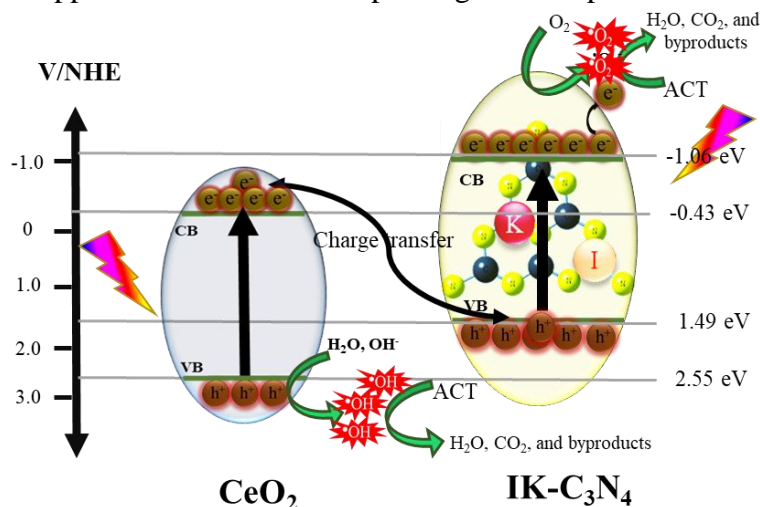


**Fig 5.** Schematic illustration of the charge transfer in a direct Z-scheme heterojunction

IK-$C_3N_4$ alone does not have the capacity to yield •OH radicals from photogenerated holes (1.49 eV) but as soon as it was paired with $CeO_2$, the oxidation potential maximizes to 2.55 eV, sufficient enough to produce these reactive radicals (2.4 eV vs NHE) (Bao and Chen, 2016). Unlike in a typical heterojunction, the holes were gathered in the VB of $CeO_2$ instead of IK-$C_3N_4$'s which is an evidence of direct Z-scheme course. The result of the experiment conforms to the calculated band positions of the two semiconductors and

confirms their capacity to directly generate reactive species, $O_2\bullet^-$ and $\bullet OH$ In addition, the radicals identified illustrate that the separation and transfer of generated $e^-/h^+$ pairs followed a Z-scheme path.

## Conclusions

In this study, we have developed a simple and facile synthesis method for the fabrication of metal/metal oxide@doped g-C$_3$N$_4$ nanocomposite for the rapid removal of nitroarenes and parmaceuticals including 4-NP, SMX and ACT. Au NPs with an average diameter of 5 – 15 nm are well deposited onto the surface of g-C$_3$N$_4$ in 3 – 6 layers structure. The as-prepared Au@g-C$_3$N$_4$ nanocomposite exhibits good catalytic properties for nitrophenol reduction in the presence of NaBH$_4$ and the reaction rate follows the order: 4-NP > 2-NP > 3-NP >2,4-DNP > 2,4,6-TNP. After the co-doping with I and K, the band structure and optical properties of IK-C$_3$N$_4$ can be fine tunes, resulting in the enhance photocataytic activity toward SMX degradation. Moreover, addition of CeO2 can shift the reaction mechanism to direct Z-scheme. More efficient charge transfer and reduced recombination of electron-hole pairs was established. Meanwhile, introduction of anions in the reaction may promote or inhibit the photocatalytic degradation depending on the concentration being added. The radical trapping experiments showed that hydroxyl radical ($^\cdot$OH), superoxide radical ($^\cdot$O$_{2^-}$) and hole (h$^+$) were all responsible for the enhanced photocatalytic degradation of pharmaceuticals. Results clearly demonstrate that g-C$_3$N$_4$ is superior photocatalyst as well as an excellent support, which can form a promising green (photo) catalyst with enormous potential of application including nitroaromatic reduction and emerging pollutant photodegradation, which provides a new venue for tailoring C$_3$N$_4$-based nanomaterials in elucidation of a wide variety of heterogeneous catalytic reactions.

[1]  Nguyen, T. B.; Huang, C. P.; Doong, R. A. (2019). Enhanced catalytic reduction of nitrophenols by sodium borohydride over highly recyclable Au@graphitic carbon nitride nanocomposites. Appl. Catal. B Environ. 240, 337-347.

[2]  De Luna, M. D. G.; Paragasb, L. K. B.; Doong, R. A. (2019) Insights into the rapid elimination of antibiotics from aqueous media by tunable C$_3$N$_4$ photocatalysts: Effects of dopant amount, coexisting ions and reactive oxygen species. Sci. Total Environ. 669, 1053-1061.

[3]  Paragas, L. K. B.; De Luna, M. D. G.; Doong R. A. (2018). Rapid removal of sulfamethoxazole from simulated water matrix by visible-light responsive iodine and potassium co-doped graphitic carbon nitride photocatalysts. Chemosphere, 210, 1099-1107.

[4]  Saha, R. S.; Lee, D. L.; Doong, R. A. (2018) Enhanced reactivity of reduced graphene oxide supported bimetallic Fe/Ni nanoparticles for trichloroethylene dechlorination, Chem. Eng. J. 334, 30-40.